





The effect of ultrasmall grain sizes on the thermal conductivity of nanocrystalline silicon thin films

Battogtokh Jugdersuren¹[✉], Brian T. Kearney², James C. Culbertson³, Christopher N. Chervin³, Michael B. Katz²², Rhonda M. Stroud³³ & Xiao Liu³³[✉]

Nanocrystallization has been an important approach for reducing thermal conductivity in thermoelectric materials due to limits on phonon mean-free path imposed by the characteristic structural size. We report on thermal conductivity as low as $0.3 \text{ Wm}^{-1}\text{K}^{-1}$ of nanocrystalline silicon thin films prepared by plasma-enhanced chemical-vapor deposition as grain size is reduced to 2.8 nm by controlling hydrogen dilution of silane gas during growth. A multilayered film composed by alternating growth conditions, with layer thicknesses of 3.6 nm, is measured to have a thermal conductivity 30% and 15% lower than its two constituents. Our quantitative analysis attributes the strong reduction of thermal conductivity with decreasing grain size to the magnifying effect of porosity which occurs concomitantly due to increased mass density fluctuations. Our results demonstrate that ultrasmall grain sizes, multilayering, and porosity, all at a similar nanometer-size scale, may be a promising way to engineer thermoelectric materials.

¹Jacobs Engineering Group, Hanover, MD, USA. ²NRC Research Associate, Naval Research Laboratory, Washington, DC, USA. ³Naval Research Laboratory, Washington, DC, USA. ✉email: jude.jugdersuren.ctr@nrl.navy.mil; xiao.liu@nrl.navy.mil

Silicon is one of the most abundant and environmentally friendly materials on earth. Despite its excellent charge carrier transport properties and dominance in the semiconductor industry, it is not yet clear if it can also become an important player in thermoelectric applications¹. A thermoelectric material would need to have a high Seebeck coefficient S , a high electrical conductivity σ , and a low thermal conductivity κ , in order to be competitive as measured by the dimensionless thermoelectric figure-of-merit (ZT), given by $ZT = S^2\sigma T/\kappa$, where T is the absolute temperature. The power factor, $S^2\sigma$, of optimally doped crystalline silicon² can be as good as materials with a much higher ZT (>1)³.

Despite its high thermal conductivity, doped silicon and its alloys have a ZT that increases almost linearly with T ^{4–6}. Silicon also has a high melting point (1414 °C). These properties could make silicon an appealing thermoelectric candidate that is usable in the ultrahigh temperature region (~ 1000 °C), where suitable thermoelectric materials are scarce^{7,8}, provided that its thermal conductivity can be reduced significantly.

In the kinetic expression, thermal conductivity can be written as:

$$\kappa = \frac{1}{3} \sum_{\text{pol.}} \int C(\omega, T) v(\omega) \Lambda_{\text{eff}}(\omega, T) d\omega \quad (1)$$

where ω is the phonon angular frequency; $C(\omega, T)$, $v(\omega)$, and $\Lambda_{\text{eff}}(\omega, T)$ are the spectral specific heat, the group velocity, and the effective mean-free path (MFP) of the phonons, respectively. Phonon dispersion determines $C(\omega, T)$ and $v(\omega)$, while $\Lambda_{\text{eff}}(\omega, T)$ depends on the phonon scattering mechanisms. The high thermal conductivity of silicon is mostly due to its large group velocity and MFP; at room temperature $\kappa \approx 150 \text{ Wm}^{-1} \text{ K}^{-1}$, the group velocity characterized by the polarization averaged speed of sound at the low-frequency limit, $v_s = 6084 \text{ ms}^{-1}$ (ref. 9), and the estimated spectral and polarization averaged MFP, $\Lambda \approx 260 \text{ nm}$, depending on the details of dispersion and modeling^{10,11}.

With the advent of nanotechnology, a steady reduction of thermal conductivity in silicon up to two orders of magnitude has been achieved using thin films^{12–14}, nanowires and nanotubes^{15–21}, nanostructures with porosity^{22–26}, and nanocrystals^{27–29}. What all of these experimental studies have in common is that in each category at least one of the relevant characteristic structural sizes L_c , either thickness, diameter, or material spacing (e.g., between adjacent voids), has approached 10–20 nm ($\sim 5 \text{ nm}$ in refs. 14,20,25,30), thus limiting $\Lambda_{\text{eff}}(\omega, T)$ close to L_c by means of phonon boundary scattering. Although modifications, such as surface roughness^{14,18}, defects^{19,21}, and composition, including oxidation^{4,17}, all affect thermal conduction, the L_c accounts for most of the experimentally observed reduction in κ ²².

A reduced group velocity has also been invoked to explain results, where κ is smaller than the amorphous limit of the corresponding material^{20,25}. The so-called minimum thermal conductivity, κ_{min} , which limits phonon MFP to no less than one-half of their wavelength, while keeping the group velocity constant at its low-frequency limit, gives a reference lower bound for a given material³¹. So far, values of κ smaller than κ_{min} at room temperature have been observed in nanocrystalline $\text{Si}_{80}\text{Ge}_{20}$ composites ($0.75 \text{ Wm}^{-1} \text{ K}^{-1}$) prepared by ball milling with average grain sizes of 9–12 nm (ref. 32), in multilayered Si/Ge nanodot thin films ($0.9 \text{ Wm}^{-1} \text{ K}^{-1}$) with layer spacings of 3 nm (ref. 33), in polycrystalline $\text{Si}_{80}\text{Ge}_{20}$ nanomeshes ($0.55 \text{ Wm}^{-1} \text{ K}^{-1}$) with pore diameters of 31 nm (ref. 24), in porous silicon nanowires ($0.33 \text{ Wm}^{-1} \text{ K}^{-1}$) with pore boundary spacing $<5 \text{ nm}$ (ref. 25), and in a number of other nanostructured materials having a characteristic structural size $L_c \leq 10 \text{ nm}$ (refs. 34–36). These

encouraging results demonstrate the potential to reduce κ further in silicon. A recent theoretical work proposes that most of the heat is transported diffusively in amorphous, as well as nanostructured solids by substituting $v(\omega)\Lambda_{\text{eff}}(\omega, T)$ in Eq. (1) with a diffusivity $D(\omega, T)$ ³⁷. This approach reduces κ_{min} by 37% or more if v is reduced.

Among those nanostructuring efforts, nanocrystallization has been the most promising approach to make silicon and silicon-germanium (SiGe) alloys into practical thermoelectric materials^{4–6,32}. Nanocrystalline silicon (*nc*-Si) is highly scalable, and can be prepared in both bulk^{4,32} and thin film forms^{5,6,38,39}, without the practical challenges associated with nanowires and nanomeshes. Even *nc*-Si material harvested from thin film processing can be pressed into bulk form in applications^{5,39}. However, only one published work of *nc*-SiGe has obtained a κ lower than κ_{min} ³² due to an exhaustive ball milling effort that reduced its grain size to 9 nm. Obviously, the success of the nanocrystallization approach depends critically on how small grain sizes can be reduced.

Grain size-dependent thermal conductivity has been studied systematically in bulk *nc*-Si for grain sizes from 550 to 76 nm, where the room temperature κ of bulk *nc*-Si decreases from 81 to $24 \text{ Wm}^{-1} \text{ K}^{-1}$ (ref. 27). Another study showed that the room temperature in-plane κ of a 1- μm thick free-suspended *nc*-Si film with grain size of 190 nm is $\sim 22 \text{ Wm}^{-1} \text{ K}^{-1}$ (ref. 28). Recently, we found that the room temperature κ of a 590-nm thick *nc*-Si thin film with grain size of 9.7 nm is $4.5 \text{ Wm}^{-1} \text{ K}^{-1}$ (ref. 29). Ultra-small grain sizes of 3 nm have been achieved by a recent epitaxial growth and oxidation approach with grains coated with a monolayer of thermal oxide, resulting in a κ of $1.1 \text{ Wm}^{-1} \text{ K}^{-1}$ (ref. 40). The strong grain size dependence of κ in *nc*-Si is a convincing piece of evidence that phonon scattering at grain boundaries dominates heat conduction, demonstrating the potential of this approach to effectively reduce thermal conductivity. Alternative and more practical *nc*-Si production methods that may reach smaller grain sizes need to be explored.

In this work, we introduce a plasma-enhanced chemical vapor deposition (PECVD) technique to produce thin films of *nc*-Si, in which the grain sizes are controlled effectively by deposition parameters, specifically by hydrogen dilution of silane. We are able to reach an average grain size of 3 nm and to generate a layered structure with layer thickness of 3.6 nm by varying the grain sizes periodically during growth. The lowest κ we reached is $0.3 \text{ Wm}^{-1} \text{ K}^{-1}$, about a factor of three below κ_{min} .

Results

Material characterizations. It has been generally accepted that hydrogen dilution plays an important role in removing disorder and reconfiguring the Si–Si network with improved structural ordering^{41,42}, although the exact growth mechanism of *nc*-Si is still debated⁴³. The ratio of flowing hydrogen (H_2) to silane (SiH_4) gases, expressed as $R = [\text{H}_2]/[\text{SiH}_4]$, is the most important film deposition parameter that determines the grain size, the crystalline content, and the porosity of the *nc*-Si in this work. For $R < 10$, the structure is still almost completely amorphous containing bonded hydrogen $\sim 10 \text{ at.}\%$ or more. As R increases, but remains <30 , nanocrystallites start to appear in the amorphous matrix with a dramatic increase in both bonded and unbonded hydrogen to as high as 20 at.%, which concentrates at the interfaces between amorphous matrix and crystalline grains. As R continues to increase >30 , the crystalline content increases rapidly and the nanograins begin to contact each other, forming heat conduction percolation paths⁴⁴. The structure transforms from mostly amorphous to mostly nanocrystalline followed by a large reduction of hydrogen concentration to $\sim 6 \text{ at.}\%$ or less^{41,42}. This

Table 1 Plasma-enhanced chemical vapor-deposited *nc*-Si film: names, parameters, and thermal conductivity at 294 K.

Sample ID	H ₂ /SiH ₄ (R)	Thickness (nm)	Dep. rate (nm min ⁻¹)	Grain size (nm)	Cry. cont. (%)	Porosity %	κ (294 K) (Wm ⁻¹ K ⁻¹)
R = 25	25	521 ± 16	5.8	3.5	30	—	1.75
R = 35	35	580 ± 22	7.3	3.8	41	—	1.47
R = 50	50	510 ± 11	5.7	3.9	45	—	1.21
R = 80	80	416 ± 34	1.8	4.2	58	2.5	1.03
R = 80/100	80/100	366 ± 26	1.4/1.2	3.3	67	7	0.71
R = 100	100	430 ± 28	1.2	3.0	73	11.5	0.84
R > 100	>100	350 ± 34	1.0	2.8	59	22	0.32

Porosity for R = 100 is estimated from R = 80 and R = 80/100. The exact R value for R > 100 could not be determined. See “Results” section for details.

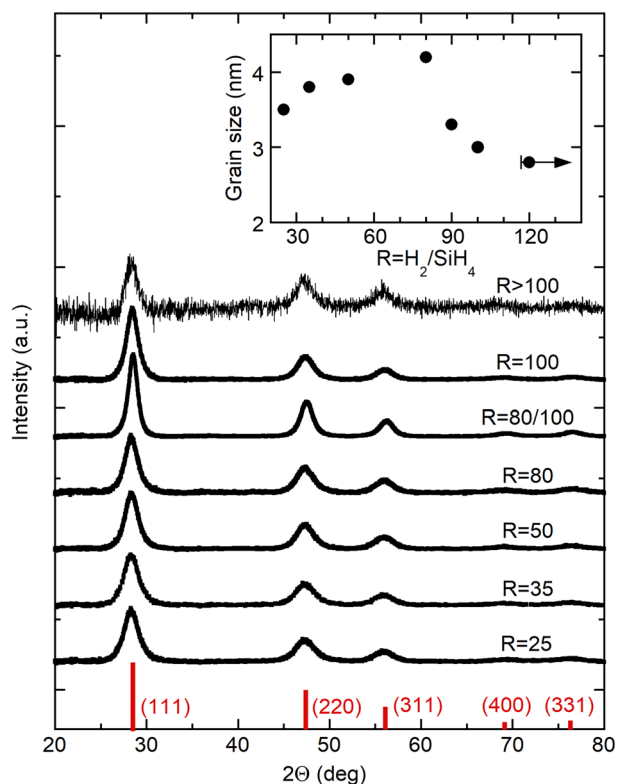


Fig. 1 Grazing-incidence X-ray diffraction patterns. For all seven plasma-enhanced chemical vapor-deposited *nc*-Si films, the backgrounds are subtracted, integrated peak areas are normalized, and y-axes are shifted for clarity. The positions and the relative peak intensities of polycrystalline silicon (ICDD no. 03-065-0565) are at the bottom for reference. The R-dependent grain size is in the inset. The right arrow indicates the uncertainty in R for the R > 100 sample explained in the “Results” section.

is the point where thermal conductivity becomes interesting and relevant to thermoelectric applications; we thus start our thermal conductivity study from R = 25 and up.

We list R, other relevant film parameters, and room temperature thermal conductivities in Table 1. The sample of R = 80/100 is a multilayered film prepared by alternating the growth condition between R = 80 and R = 100 for 51 times with each layer thickness of 3.6 nm. The sample with R > 100 was made with a reduced SiH₄ flow below its control limit and its exact R is unknown. Despite their varying amorphous content, we call all of our PECVD-grown films *nc*-Si for simplicity. Technically, these films are structurally different from those studied in refs. 27,28, and should be called hydrogenated *nc*-Si or

nc-Si:H, due to their incorporation of hydrogen. For convenience, we drop “hydrogenated” in this article.

Figure 1 shows the grazing-incidence X-ray diffraction (XRD) results of all seven PECVD films after background subtraction. The five diffraction peaks are associated with the (111), (220), (311), (400), and (331) planes of silicon. Their positions and relative peak intensities are in good accordance with the diamond cubic crystal structure of silicon (ICDD no. 03-065-0565; plotted at the bottom for reference), indicating no preferred orientation for all films. The data for R > 100 is much noisier than the others due to its smaller film thickness and lower diffracting volume. The R dependence of the average grain sizes, calculated from the three main peaks at (111), (220), and (311), using the Scherrer equation, is shown in the inset where we assign R = 90 for the film with R = 80/100 and represent the R > 100 film with a right arrow. The same conventions are used for the rest of the paper. The average grain size increases with R starting when the film is predominantly amorphous (R = 25) and reaches a maximum at R = 80, when the structure is mostly nanocrystalline. This trend is similar to what we have observed earlier in *nc*-Si films prepared by hot-wire chemical vapor deposition (HWCVD)⁴⁴. However, the grain size of the PECVD films increases only by ~50% at most and remains within the range of 3–4 nm. This contrasts with the R dependence in HWCVD films, where the average grain size increases by a factor of 4 and reaches 9 nm at its maximum. Depending on deposition conditions, a wide range of grain sizes have been produced with PECVD⁴². The ability to produce ultrasmall grains makes PECVD-grown *nc*-Si films an appealing material for thermal conductivity studies and for potential thermoelectric applications.

The results of Raman spectra are shown in Fig. 2a for all seven PECVD films. A peak at ~510 cm⁻¹ associated with transverse optical modes is visible for all films, even for R = 25, indicating the appearance of the crystalline phase, consistent with the XRD results shown in Fig. 1. A faint peak at ~615 cm⁻¹ caused by vibrations of Si–H bonds is also visible. In order to estimate their crystalline content, we use three Gaussian peaks located at 480, 505, and 520 cm⁻¹ to fit the Raman spectra, which originate from the amorphous, grain boundary, and crystalline phases, respectively. An example of the fitting process for R = 100 is shown in Fig. 2b. We calculate the integrated areas of the three peaks weighted by the scattering cross-section ratio for amorphous and crystalline silicon, which depends on grain sizes listed in Table 1. The crystalline content is approximated by the ratio of the combined weighted areas of both grain boundary and crystalline peaks to the total weighted areas of the three peaks; the results are shown in Fig. 2c. The crystalline content increases rapidly with R reaching a maximum of 73% at R = 100 and drops again for R > 100. Similar R dependence has previously been observed in PECVD- and HWCVD-grown Si films^{42,44}. Upon closer inspection of the crystalline peak, one finds it is shifted to the right

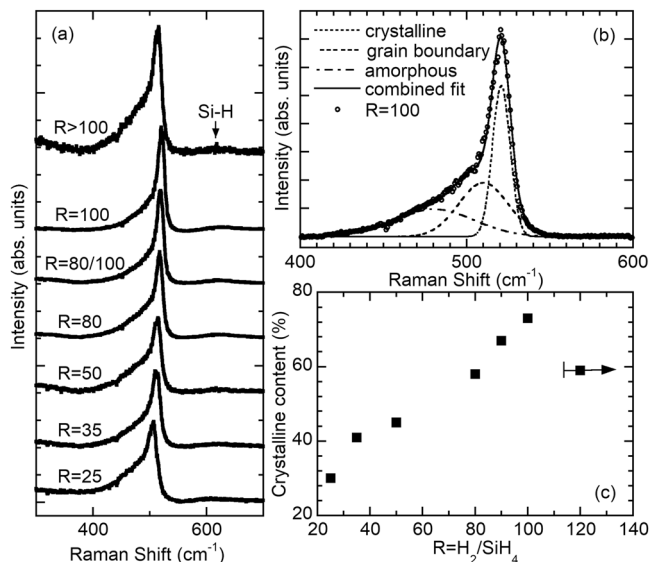


Fig. 2 Raman spectra: intensity vs. Raman energy shift. **a** Raman spectra of all seven plasma-enhanced chemical vapor-deposited *nc*-Si films. The *y*-axes are shifted for clarity. A faint peak at $\sim 615\text{ cm}^{-1}$ caused by vibrations of Si-H bonds is indicated. **b** The empirical fittings for $R = 100$. Contributions from amorphous, grain boundary, and crystalline phases are shown separately. **c** The crystalline content vs. R for all seven films. The right arrow indicates the uncertainty of R for $R > 100$ explained in the “Results” section.

progressively from $R = 25$ up to $R = 80$ – 100 . For $R > 100$, this trend is reversed. The redshift of Raman crystalline peak with decreasing grain size has been associated with the phonon confinement effect due to phonon localization in nanocrystals⁴⁵. Thus, the concomitant R dependence on grain size and crystalline content in our PECVD *nc*-Si films demonstrate the effect of controlling hydrogen dilution in both promoting crystalline growth and limiting the grain size.

Figure 3 shows the high-angle annular dark-field images (HAADF) of cross-sectional scanning transmission electron microscopy (STEM) for three films: $R = 80$ in Fig. 3a–c grown on silicate glass, $R = 80/100$ in Fig. 3d–f and $R > 100$ in Fig. 3g–i, both grown on single-crystal silicon. A columnar growth structure can be observed in the lower magnification images in Fig. 3a, d, which is not obvious in Fig. 3g. Note that the white dots in upper part in Fig. 3g are artifacts due to the STEM cross-section preparation. Unlike the HWCVD-grown *nc*-Si films studied earlier, PECVD films have no amorphous incubation layer and silicon nanocrystallites grow almost instantaneously on substrates. This is advantageous in terms of thermoelectric applications. The higher magnification images in Fig. 3c, f, i reveal lattice planes within individual 2–5 nm crystallites, demonstrating that the crystallites are randomly oriented. This is in agreement with the XRD results, despite the columnar growth structure that is related to density variation. A particularly interesting point is that in Fig. 3e, we can clearly see the layered structure due to the alternation of deposition conditions between $R = 80$ and 100. The visible thickness is also consistent with measurements from the N&K Spectrophotometer. The HAADF intensity variation also indicates that the films are not fully dense. Pores between grains are visible as dark regions without visible lattice planes in the higher magnification images. The image intensity across the film–substrate interface provides a basis for estimation of the film porosity, at 2.5%, 7%, and 22% for the $R =$

80, $R = 80/100$, and $R > 100$ samples, respectively, also listed in Table 1.

Thermal conductivities. The temperature-dependent thermal conductivity results $\kappa(T)$, measured by differential 3ω method (see “Methods” section), of all seven films are shown in Fig. 4. Additional time-domain thermoreflectance (TDTR) experiments were performed on $R = 80$ at University of Illinois (Urbana-Champaign) to measure its longitudinal speed of sound and to verify 3ω results, which are within 5% (smaller than the thickness uncertainty mentioned later)⁴⁶. For comparison, the results of five HWCVD films we studied earlier are included^{29,44}. Also plotted are κ of a 0.52- μm thick sputtered *a*-Si film grown at 230 °C (ref. 47). It represents the thermal conductivity of a typical *a*-Si film, as the κ of a variety of *a*-Si films fall within a narrow range of it, such as a 0.6- μm thick HWCVD *a*-Si²⁹ and a 0.13- μm thick electron-beam evaporated *a*-Si⁴⁸, although some special type of HWCVD *a*-Si can exhibit much higher κ ^{49,50}. The $\kappa_{\text{min}}^{\text{D}}$ and $\kappa_{\text{min}}^{\text{BvK}}$ curves are the conventional minimum thermal conductivity calculated, using the Debye dispersion and an alternative one that takes a reduction of the group velocity of high-frequency phonons into account (to be introduced later). On the top *x*-axis, we show the dominant phonon wavelength $\lambda_{\text{dom}} = v_s/v_{\text{dom}}$, responsible for heat transport at T , where $v_{\text{dom}} = 90[\text{GHz K}^{-1}]T$ is the frequency of dominant heat carrying phonons.

In the temperature range investigated, grain boundary scattering dominates the thermal transport as in the HWCVD films^{29,44}. This is evident from the small values of κ and their overall positive temperature dependence. However, the R dependence of PECVD films is dramatically different from that of HWCVD films. While most of HWCVD films have a κ higher than the *a*-Si, all PECVD films have a κ lower than the *a*-Si. To demonstrate the difference, a comparison of the R -dependent κ at $\sim 294\text{ K}$ between HWCVD and PECVD is shown in Fig. 5, on the top and bottom *x*-axes, respectively, because different ratios of R are required to reach the onset of crystallinity⁵¹, depicted by a vertical blue bar. The room temperature κ of a typical *a*-Si film, $\kappa_{\text{min}}^{\text{D}}$ and $\kappa_{\text{min}}^{\text{BvK}}$ shown in Fig. 4, and $\kappa_{\text{min}}^{\text{Diff}}$ from ref. 37 are presented as solid or patterned horizontal red lines. Starting from the small R , where the film is mostly amorphous, κ increases with R for HWCVD, but decreases for PECVD. In HWCVD, κ reaches a maximum at $R = 8$ and goes down for $R = 10$. For PECVD, κ decreases monotonically with R ; passes $\kappa_{\text{min}}^{\text{D}}$ at $R = 80$, and drops below $\kappa_{\text{min}}^{\text{BvK}}$ for $R > 100$. An interesting observation is that the κ of $R = 80/100$ is 30% and 15% lower than $R = 80$ and $R = 100$, respectively, although both its average grain size and crystalline content are in-between. This suggests that alternating the grain sizes at an interval of 3.5 nm further reduces heat conduction despite an otherwise polydispersed grain distribution is not expected to affect grain boundary scattering much⁵². The most remarkable observation is that the κ of $R > 100$ is more than a factor of five smaller than that of *a*-Si and a factor of three smaller than the amorphous limit of silicon, $\kappa_{\text{min}}^{\text{D}}$. Compared to all previous results, this is achieved with a very modest porosity.

As the crystalline content in both HWCVD and PECVD increases with R in a similar way (see Fig. 3 in ref. 44 for HWCVD), it is obvious that the different R dependence of κ can be explained by the greatly reduced grain sizes in PECVD. In HWCVD, the increase of κ with R has been interpreted with an enhancement in nanocrystalline percolation paths that outweighs the increased interface scattering⁴⁴. In PECVD, the opposite would be true. The reduction in grain sizes greatly increases the grain boundary content and hence their scattering of heat

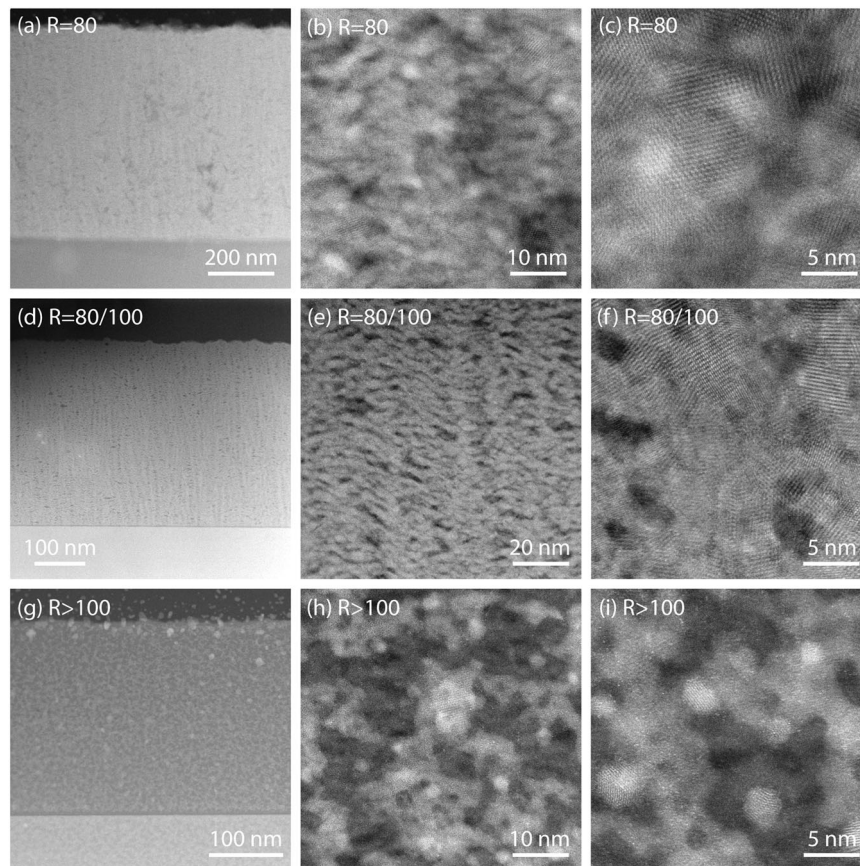


Fig. 3 High-angle annular dark-field images of cross-sectional scanning transmission electron microscopy. Three plasma-enhanced chemical vapor-deposited *nc*-Si films with $R = 80$ in **a-c**, $R = 80/100$ in **d-f**, and $R > 100$ in **g-i** are shown. The white particles extending into the glue line above the film in **g** are redeposition artifacts from the ion milling preparation. Scale bars are given at the bottom of each image.

carriers. It affects boundary scattering transmissivity and specularity, as well as the speed of sound, rendering crystalline percolation paths devitalized. Studies show that high-frequency phonons or diffusive modes, which are dominant heat carriers at room temperature and above, are particularly sensitive to a reduction of L_c ^{33,36}.

We note that although the *nc*-Si films studied in this work are hydrogenated with varying hydrogen content, we don't think the inclusion of hydrogen or hydrogen bonds plays a meaningful role in thermal conduction. In our previous HWCVD *nc*-Si films, removal of hydrogen by a 600 °C anneal increases κ by 35%, mostly attributable to an increase in grain size²⁹. In addition, no hydrogen content dependence has been found in thermal conductivity of sputtered *a*-Si with H varying from 1 to 20 at.% (ref. 47).

Analytical modeling. In order to preserve their ultras-small grain sizes for the interest of the thermal conduction study, none of the PECVD films are annealed to remove their amorphous content. At $R > 80$, their crystalline content reaches ~60% and grain boundary scattering is expected to dominate heat conduction. We extend the model of grain boundary scattering with the Born-von Karman (BvK) dispersion to examine whether this approach is still adequate to explain our results. In our previous work on HWCVD *nc*-Si with a grain size of 9.7 nm, we also used the Debye and the Morelli-Callaway dispersions²⁹. As the Debye model fails to give a satisfactory fit and the Morelli-Callaway model gives a result similar to BvK's, we only focus on the BvK dispersion in this work, as it is also considered to be most accurate among analytical models¹¹. We previously considered

both frequency-dependent and -independent grain boundary scattering²⁹. However, as pointed out by Wang et al.²⁷, the frequency-dependent model only affects the heat conduction of low-frequency phonons at $T < 100$ K. We only consider the frequency-independent (gray) grain boundary scattering in this work, which gives phonon MFP $\Lambda_B(\omega)$ as,

$$\Lambda_B(\omega) = \alpha D, \quad (2)$$

here α and D denote a fitting parameter and the average grain size, respectively. In addition, we also include impurity/defect scattering and Umklapp scattering as detailed in Methods section.

For the demonstration purposes, we apply the model to $R = 80$ ($D = 4.2$ nm) and $R > 100$ ($D = 2.8$ nm), representing the largest and smallest D in this work, respectively. Both films also have relatively high crystalline content. Their BvK thermal conductivity results are shown in Fig. 6 together those of $D = 76$ (ref. 27) and 9.7 nm (ref. 29). We thus demonstrate that it is possible to describe the temperature-dependent κ of *nc*-Si with grain sizes varying by two orders of magnitude from 550 to 2.8 nm with a single set of parameters, where the only grain size-dependent parameter is α . As we noticed earlier in HWCVD *nc*-Si, the measured κ rises with increasing temperature stronger than a typical *a*-Si and BvK modeling. Similar behaviors have been observed in epitaxially grown *nc*-Si thin films with 3–40 nm grains coated with a monolayer of thermal oxide⁴⁰. Higher temperature measurements would help to show how far this trend continues.

Figure 7 summarizes the room temperature κ vs. grain size D for *nc*-Si studied so far, including the HWCVD *nc*-Si thin films^{29,44}, the bulk *nc*-Si²⁷, the polycrystalline Si thin films²⁸, the

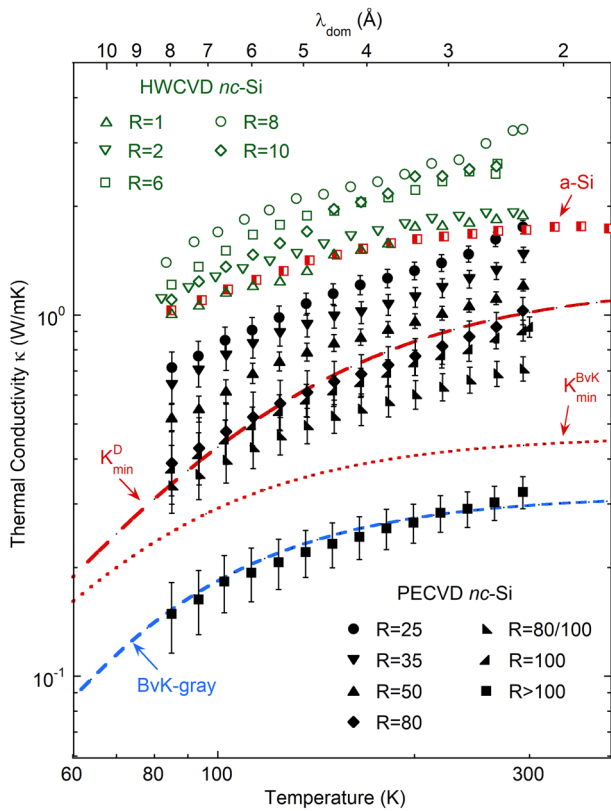


Fig. 4 Thermal conductivity vs. temperature. The data of all seven plasma-enhanced chemical vapor-deposited *nc*-Si films are compared with those of five hot-wire chemical vapor-deposited *nc*-Si films⁴⁴, and a sputtered *a*-Si film, 0.52 μm thick, grown at 230 °C (ref. 47). The computed minimum thermal conductivities, κ_{\min}^D (dashed red line) and κ_{\min}^{BvK} (dotted red line), which utilize Debye or Born-von Karman dispersion relationships, respectively, are explained in the minimum thermal conductivity section. The fitting curve for $R > 100$ using the Born-von Karman dispersion relation and frequency-independent (gray) grain boundary scattering explained in the test are shown as a dashed blue line. The error bars for plasma-enhanced chemical vapor-deposited *nc*-Si films are representative of standard deviations of thermal conductivity measurements and uncertainties in film dimensions, as discussed in detail in Supplementary Note 2.

epitaxial *nc*-Si⁴⁰, and the PECVD *nc*-Si thin films presented in this work. The overall trend resembles those modeled in refs. 25,30,53,54; approaching saturation for $D > 100$ nm and decreasing steadily for $D < 10$ nm. However, we didn't observe the expected $\kappa \propto D$ at the small D limit³⁶. The reason may be that the α we obtained by least squares fitting decreases with D , e.g., we have $\alpha = 0.26$ and 0.15 for $D = 4.2$ and 2.8 nm, respectively. This trend has been observed at larger grain sizes as well^{27,29}. So it is likely that the presumed linear dependence is not sufficient to describe the enhanced grain boundary scattering with decreasing D and a reduction in α compensates the deficiency. To improve our modeling, we set $\Lambda_B(\omega) = \Lambda_B$ as a fitting parameter in Eq. (10) and plot it vs. D in the inset of Fig. 7 covering three orders of magnitude. Here, we only use those data from the bulk, HWCVD and PECVD for which the values of α have been determined. We find that a superlinear dependence, as

$$\Lambda_B = (0.17 \pm 0.05)D^{1.3 \pm 0.1}, \quad (3)$$

best describes the grain size dependence shown by the solid straight line. Replacing Eq. (2) with Eq. (3), we obtain κ_{BvK} vs. D

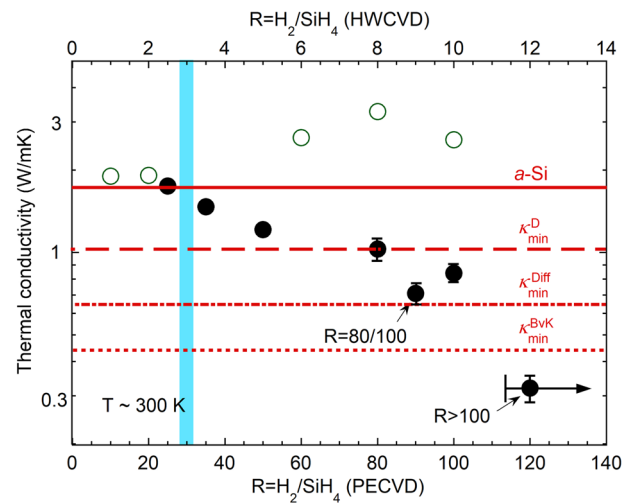


Fig. 5 The R dependence of thermal conductivity κ at -300 K. Data of hot-wire chemical vapor-deposited (green open circle) and plasma-enhanced chemical vapor-deposited (black solid circles) *nc*-Si films are compared. The R values for hot-wire chemical vapor deposited and plasma-enhanced chemical vapor deposited are on the top and bottom axes, respectively. The right arrow indicates the uncertainty of R for $R > 100$ explained in the “Results” section. The vertical blue bar represents the R range beyond which the films become mostly crystalline. The room temperature κ of a sputtered *a*-Si film, 0.52 μm thick, grown at 230 °C (ref. 47) and the two κ_{\min} shown in Fig. 4 and an additional diffusive κ_{\min}^{Diff} (ref. 37) are presented as patterned horizontal red lines. The error bars for plasma-enhanced chemical vapor-deposited *nc*-Si films are given (unless they are smaller than the data points), as discussed in detail in Supplementary Note 2.

at room temperature in Fig. 7, as shown by the solid line. Thus, our simple kinetic analysis gives a qualitative description of both temperature and grain size dependence of *nc*-Si. In order to compare with those common empirical expressions in refs. 25,30,53,54, we express κ_{BvK} vs. D as

$$\kappa = \left(\frac{1}{0.12D^{1.3}} + \frac{1}{\kappa_{rest}} \right)^{-1}, \quad (4)$$

where $\kappa_{rest} = 145 \text{ Wm}^{-1} \text{ K}^{-1}$ represents the large grain asymptotic limit of κ , which is close to the value of crystalline silicon and $\kappa \approx 0.12D^{1.3}$ (here κ is in unit of $[\text{Wm}^{-1} \text{ K}^{-1}]$ and D in $[\text{nm}]$) is the small grain size limit at $D < 10$ nm. As α is determined by the the transmissivity t and specularity p of phonons traveling perpendicular and parallel to an interface respectively, and has been shown in Si/Ge superlattice nanowire that^{9,27}

$$\alpha^{-1} = \left(\frac{3t/4}{1-t} \right)^{-1} + \left(\frac{1+p}{1-p} \right)^{-1}, \quad (5)$$

it is reasonable to understand that a decrease of both t and p with D may be the source of grain size dependence of α .

Minimum thermal conductivity. The minimum thermal conductivity is a reference lower bound for a given material, signaling that a minimum in phonon MFP has been reached at a given frequency ω due to localization. Thermal conductivity smaller than κ_{\min}^D would suggest that mechanisms other than a reduction of Λ_{eff} take effect, such as a reduction in phonon density of states and/or speeds of sound.

In our previous study, we found that κ of *nc*-Si approaches that of *a*-Si with decreasing grain size and concluded that κ of *nc*-Si does not differ much from that of *a*-Si^{29,44}. This observation is supported by molecular dynamic simulations, showing that κ

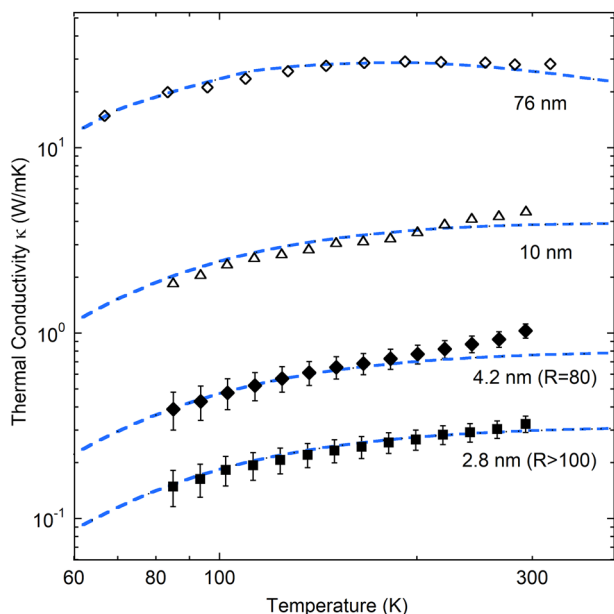


Fig. 6 Fitting thermal conductivity vs. temperature. Two plasma-enhanced chemical vapor-deposited *nc*-Si films, $R = 80$ and $R > 100$, with the average grain sizes of 4.2 and 2.8 nm, respectively, are shown together with a hot-wire chemical vapor-deposited and annealed *nc*-Si film with grain size of 9.7 nm (ref. ²⁹) and a bulk *nc*-Si sample with grain size of 76 nm (ref. ²⁷). The fitting curves using the Born-von Karman dispersion and frequency-independent (gray) grain boundary scattering explained in the “Analytical modeling” section are shown in dashed blue lines. The error bars for plasma-enhanced chemical vapor-deposited *nc*-Si films are given, as discussed in detail in Supplementary Note 2.

decreases almost linearly with D and approaches that of *a*-Si for $D = 2\text{--}3$ nm (refs. ^{55,56}). In this work, we demonstrate that with a further reduction of grain sizes the κ of many PECVD *nc*-Si films becomes smaller than that of *a*-Si and the amorphous limit, thus questioning such similarity. Indeed, Wingert et al. found that the κ of crystalline Si nanotubes with wall thickness of ~ 5 nm is 30% smaller than that of *a*-Si nanotubes with the same dimensions²⁰. Studies of nanostructured *a*-Si confirm that the amorphous limit is approached but not broken by *a*-Si with decreasing L_c to ~ 5 nm (ref. ^{57,58}). It appears that the characteristic structural size, which dominates nanostructured crystalline materials, is not as important for *a*-Si.

In *a*-Si, heat is conducted approximately equally by propagating modes with MFP up to $1\ \mu\text{m}$, called propagons, and interactive nonpropagating modes with a MFP on the order of interatomic spacings, called diffusons⁵⁹. In principle, a similar heat conduction mechanism applies to *nc*-Si with small grain sizes⁵⁵. However, Zhao et al. studied κ of polycrystalline nanowires with grain sizes from ~ 1 to 3.5 nm, using molecular dynamics simulations and found κ can be reduced to one-third of *a*-Si nanowires having the same structure dimensions⁶⁰. Their detailed spectroscopic analysis shows a severe reduction of heat conduction in the effective phonon MFP range of $\sim 0.2\text{--}3$ nm, pointing to a strong reduction of propagon contribution to heat conduction in *nc*-Si. They suggested that the presence of grain boundaries disrupts the continuity of atomic bonds causing an increased scattering and a decreased velocity of propagons, consistent with our observations. What is still unclear and beyond the scope of molecular dynamics simulations is the contribution of propagons with wavelength larger than the simulated structure and grain sizes. The strong grain size dependence observed in this work indicates their contributions to be minimal. We suggest that

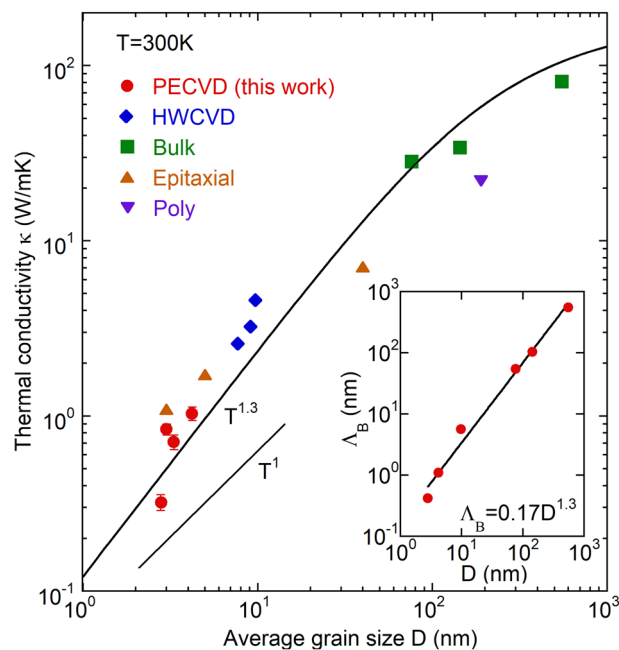


Fig. 7 The room temperature thermal conductivity vs. the average grain size D . The hot-wire chemical vapor-deposited *nc*-Si thin films^{29,44}, the bulk *nc*-Si²⁷, the polycrystalline silicon²⁸, the epitaxial *nc*-Si⁴⁰, and the plasma-enhanced chemical vapor-deposited *nc*-Si thin films presented in this work are compared. The solid curve is the result of the Born-von Karman model calculation using the empirical superlinear D -dependent phonon mean-free path shown in the inset and explained in the “Analytical modeling” section. It is in contrast to the reference line labeled T^{-1} at the small D end. The error bars for plasma-enhanced chemical vapor-deposited *nc*-Si films are given (unless they are smaller than the data points), as discussed in detail in Supplementary Note 2.

the combination of a polydispersed grain distribution and the occurrence of density fluctuation or porosity (to be discussed below) may have reduced their contribution. A detailed frequency-dependent thermal conductivity study may help to provide more insights⁴⁹.

A comparison of Debye and BvK models in analyzing κ of *nc*-Si^{27,29} demonstrate that the Debye model overestimates the contribution of high-frequency phonons by about a factor of two at room temperature. Thermal conductivity smaller than κ_{\min}^D has been observed in an increasing body of nanostructured materials in recent years^{24,32–36}. While changes other than phonon MFP may account for some of the observations, overestimation of high-frequency phonon group velocity may have contributed to some of them^{20,36}.

In this work, we insert the same $\Lambda_{\text{eff}}(\omega, T) = \pi v_s / \omega$ as in κ_{\min}^D , the smallest allowable phonon MFP at a given frequency ω , into Eq. (9) in “Methods” section to obtain the minimum thermal conductivity by the BvK dispersion, $\kappa_{\min}^{\text{BvK}}$. The result is shown in Figs. 4 and 5 together with the standard κ_{\min}^D with the Debye dispersion. This means that if a more realistic dispersion is used, no violation of Ioffe-Regel criterion nor other mechanisms would be needed for most PECVD *nc*-Si films except for $R > 100$. Our $\kappa_{\min}^{\text{BvK}}$ is also lower than the diffuson-dominated thermal conductivity limit $\kappa_{\min}^{\text{Diff}}$ ³⁷, also shown in Fig. 5.

So far, we have not taken a reduction of sound speeds due to nanostructuring into account as has been observed in some recent studies, as a result of reduced structure size²⁰ or increased porosity²⁵. The TDTR measurement on $R = 80$ shows that its longitudinal speed of sound is only $\sim 50\%$ of the bulk silicon. If we

reduce v_s by half (assuming both v_l and v_t reduce proportionally), $\kappa_{\text{min}}^{\text{BvK}}$ and $\kappa_{\text{min}}^{\text{Diff}}$ would be reduced by 42% and 50%, respectively. This is lower than the measured κ of all our PECVD films and we expect sound speeds in $R = 100$ and $R > 100$ would be even lower.

The effect of porosity. At $R = 80$, porosity starts to appear in HAADF and it reaches 22% for $R > 100$. According to molecular dynamics simulations, porosity reduces κ by a reduction in phonon conduction channels and an increase in phonon scattering at the pore surfaces^{61,62}. Crystalline silicon with high porosity (64–89%) has pushed down κ to as low as $0.04 \text{ W m}^{-1} \text{ K}^{-1}$ (ref. ⁶³). Single-crystalline silicon nanowires with 43% porosity have reached κ of $0.33 \text{ W m}^{-1} \text{ K}^{-1}$ (ref. ²⁵). In contrast to early theories where porosity is the only parameter, many experiments suggest a strong size effect on κ , such as pore sizes and their spacings^{23,24,26,30,64–66}.

For a quantitative analysis, we first apply the phonon-hydrodynamics approach which considers both the porosity φ and structure size L_c (grain or pore) and κ_{eff} is given by refs. ^{65,67}

$$\kappa_{\text{eff}} = \kappa \left[\frac{1}{(1 - \varphi)^3} + \frac{9\varphi(1 + 3\sqrt{\varphi/2})K_n^2}{2(1 + C'K_n)} \right]^{-1}, \quad (6)$$

where $C' = 2C_1 + C_2 \exp(-\gamma/K_n)$ and the Knudsen number $K_n = \Lambda/L_c$ is the ratio of phonon MFP of silicon and its structure size. So the first and the second terms in the parenthesis reduce κ_{eff} by an increase of φ or K_n , respectively. This quantitative evaluation depends on the choice of parameters C_1 , C_2 , γ , and even Λ ^{65,67}. We use $C_1 = 0.864$, $C_2 = 0.290$, $\gamma = 1.25$, and $\Lambda = 40$ nm for our $R > 100$ film as in ref. ⁶⁵, where $L_c = 1\text{--}2.8$ nm as the size range of porous regions are generally smaller than D (Fig. 3h–i). We reach $\kappa_{\text{eff}} = 2.1\text{--}5.8 \text{ W m}^{-1} \text{ K}^{-1}$. A Monte Carlo simulation work that considers an array of parallel pores along the heat conduction direction shows κ decreases not only with increasing porosity, but also with decreasing pore size as $L_c < 10$ nm (ref. ⁶⁶). However, κ remains above $\sim 1 \text{ W m}^{-1} \text{ K}^{-1}$ even when $\varphi = 30\%$ and $L_c = 0.5$ nm. Therefore both approaches, although completely different, severely underestimate the observed reduction of κ in our PECVD *nc*-Si. This suggests that a combination of the above discussed effects (grain size, phonon softening, and porosity) may have enhanced the reduction in κ .

Discussion

It would be desirable if all the factors encountered in this work could be analyzed in a comprehensive model. Recent theoretical work suggests hierarchical nanostructuring involving nanograins, multilayering and voids can all be beneficial to the power factors⁶⁸. It is worth mentioning that the grain size reduction from $R = 80$ to $R > 100$ is $\sim 50\%$, but the reduction of κ is more than a factor of 3. The multilayered structure in $R = 80/100$ shows that a polydispersed grain distribution is effective, but this has so far not been understood theoretically. The low κ is further aided by an emergence of porosity and a reduction of sound speeds. However, neither a higher porosity²⁵ nor a larger reduction of sound speeds²⁰ yields a smaller κ in silicon than shown in this work. Based on our STEM observation, we find the porosity in PECVD *nc*-Si manifests more as isolated low-density regions than actual pores with sizes no larger than the crystalline grains. It is likely that such a density fluctuation is more effective than pores in disrupting heat conduction, via either propagons or diffusons. We thus attribute the strong reduction of κ , as well as v_s , to the magnifying effect of increased porosity that originates from the density fluctuation in our high R PECVD films to the effect of ultrasmall grain sizes, in agreement with recent Monte Carlo simulations⁶⁹.

To summarize, we show nanocrystallization by hydrogen dilution using PECVD and HWCVD has quite different effects in terms of the resulting grain sizes and thermal conductivity. The smaller grain sizes and the lower thermal conductivities achieved by PECVD make this material a compelling choice for thermoelectric applications. We find that a superlinear dependence of phonon MFP on the average grain size best describes grain boundary scattering for grain sizes varying more than two orders of magnitude from 2.8 to 550 nm. With that, we provide a consistent description of both temperature and grain size dependences with the BvK dispersion. The observation that κ of a multilayered *nc*-Si is smaller than its two constituents not only emphasizes the importance of boundary scattering, but also reminds us of the limitation of our current analytical modeling in dealing with a broad or nonuniform distribution of grain sizes. Our results support a different heat conduction mechanism between nanocrystalline and amorphous materials due to the strong characteristic structural size dependence observed in the former. The origin of such difference is not known and more studies are needed. Applying the BvK dispersion to the minimum thermal conductivity effectively lowers its value by more than a factor of two. This evaluation method allows a reduction of the group velocity of high-frequency phonons, while keeping phonon MFP not smaller than half of their wavelength, a key criteria of minimum thermal conductivity³¹. Compared with the similarly low values of κ achieved in silicon²⁵, our *nc*-Si films have a rather low level of porosity that is the natural consequence of our film production process. We conclude that the low κ achieved in this work is due to a combination of ultrasmall grain size, and the appearance of a density fluctuation at the same length scale of their grain sizes. We therefore propose that ultrasmall grain sizes, multilayering, and a moderate amount of porosity, all at comparable size scales, may be the ideal ingredients to control heat conduction in thermoelectric materials.

Methods

Thin film preparation. Thin films of *nc*-Si were prepared by PECVD with an Oxford PlasmaPro100 system. For all depositions, the chamber pressure was maintained at 700 mTorr and the substrate temperature was held at 250 °C with a radio-frequency (13.56 MHz) plasma power of 90 W. Films were grown on sapphire, single-crystal silicon, and borosilicate substrates for 3ω thermal conductivity measurements and structural characterizations. Besides R , other deposition parameters, such as chamber pressure, plasma power, and substrate temperature, have effects as well^{43,70}. We optimized and kept them constant in this work. The desired R was achieved by throttling $[\text{H}_2]$ in the range from 25 to 100 s.c.c.m., while keeping $[\text{SiH}_4] = 1$ s.c.c.m.. As the flow rate for both H_2 and SiH_4 can only be adjusted between 1 and 100 s.c.c.m. in this system, the R value is limited to a maximum of 100. Most of the films were prepared with a constant R between 25 and 100. One film was prepared by alternating the growth condition between $R = 80$ and $R = 100$, for a growth time of 160 and 190 s, respectively, in each cycle based on a predetermined growth rate to reach 3.6 nm thickness for each layer. The process was repeated 51 times, resulting in a multilayered structure with varying grain sizes over a total thickness of 366 nm. Another film was targeted to grow at $R = 100$. However, an unintentional mechanical problem caused a reduced SiH_4 flow by an unspecified amount, resulting in an effective R that is larger than 100. We include this film for its significant reduction of κ . Systematic investigation of hydrogen dilution for $R > 100$ is, however, a subject of future study.

Film thickness was measured with an N&K Spectrophotometer at locations where 3ω thermal conductivity measurements took place. The results were verified by stylus profilometry on selected films after a photolithography and reactive-ion etching process to create a depth profile. The results agree to within 8%, which constitutes one of the main sources of error in the thermal conductivity evaluation.

Experimental. Although R -dependent studies of PECVD-grown *a*-Si and *nc*-Si abound^{41–43,70}, we start with a detailed structural characterizations of our films. XRD measurements were performed with a Rigaku SmartLab X-ray diffractometer using fixed $\text{CuK}\alpha$ radiation in parallel-beam mode. The Raman spectra were acquired with a home-built micro-Raman setup using a single-mode 488 nm laser with typical spot size $< 1 \mu\text{m}$ and power ~ 0.5 mW at the sample. Cross-sectional STEM studies of selected films were performed with a Nion UltraSTEM 200-X operated at 200 kV. HAADF images were collected with a nominal probe size of 120 pm, and probe current of 100 pA. Estimates of the film porosities were

obtained from quantitative analysis of the HAADF image intensity, using the growth substrate as an in situ intensity calibration standard. The estimates included an assumption that variations in sample thickness across the interface are negligible, and the crystallite density is equivalent to bulk silicon. Two of the films ($R = 80$ and $R = 80/100$) were prepared by focused ion beam lift-out with a Helios G3 FIB, while the third ($R > 100$) was prepared by conventional mechanical polishing and low-angle Ar ion milling with a Fischione Nanomill.

To measure κ , we employed the differential 3ω method which was established by Cahill et al.⁴⁷ More details are given in Supplementary Note 1. A planar metal line, made of 5 nm Ti/120 nm Au, was deposited directly on the surface of the *nc*-Si thin film by a photolithography and lift-off process, see Supplementary Fig. S1. This patterned metal film served as both a heater and a thermometer, which supplied an AC current with a frequency ω in the range 3–1500 Hz and probed temperature oscillations in the film generated by an AC current at 3ω . This temperature oscillations is proportional to the sum of the thermal resistances of the film, the sapphire substrate, and their interface. The contribution from sapphire substrate can be subtracted as it is measured separately in the absence of a film, the contribution of which to the total varies from 10% at 85 K and 1500 Hz to 70% at 294 K and 3 Hz, see Supplementary Fig. S2. The interface thermal resistance is not known and is assumed to be negligible. This is based on the lack of significant thickness dependence of similarly prepared films and the excellent agreement between results on the same $R = 80$ sample obtained with 3ω and TDTR measurements, where thermal waves are confined to the film and no interfacial effect should exist. Four 3ω devices were fabricated together on each sample, with nominal metal film length of 1.2 mm and width of 10, 15, 20 and 30 μm . The exact length and width were determined after fabrication under a calibrated microscope. Thicknesses of our films were much smaller than the heater width, satisfying the one-dimensional heat flow condition of the differential 3ω technique. For confirmation purposes, most of the films were measured with more than one device and the differences in measured κ are typically within error bars given in Supplementary Note 2, where more details of the error estimation are given.

BvK model. The BvK model considers a realistic phonon dispersion that flattens at the end of the Brillouin zone⁹, which can be modeled as

$$\omega = \omega_0 \sin(\pi q/2q_0). \quad (7)$$

Here, we choose the cutoff wave vector to be the same as used in the Debye model, $q_0 = \omega_D/v_s$, where ω_D is the Debye frequency. That leads to a cutoff frequency of $\omega_0 = 2\omega_D/\pi$, so that we retain the same number of phonon modes and $v(\omega)$ remains the same as in the Debye model at low frequencies. From Eq. (7), the phonon group velocity is written as

$$v(\omega) = v_s \cos(\pi q/2q_0). \quad (8)$$

Compared with the Debye model, the velocity of high-frequency phonons is reduced and at the Brillouin zone edge $v(\omega_0) = 0$.

The BvK thermal conductivity is²⁹:

$$\kappa_{\text{BvK}} = \frac{2\hbar^2 q_0^2}{\pi^4 k_B T^2} \int_0^{\omega_0} \Lambda_{\text{eff}}(\omega, T) \frac{\omega^2 \exp(\hbar\omega/k_B T) [\sin^{-1}(\omega/\omega_0)]^2 d\omega}{(\exp(\hbar\omega/k_B T) - 1)^2}, \quad (9)$$

where k_B denotes the Boltzmann constant, and \hbar the reduced Planck's constant. According to Matthiessen's rule, $\Lambda_{\text{eff}}(\omega, T)$ combines phonon scattering mechanisms, such as impurity/defect scattering $\Lambda_I(\omega)$, Umklapp scattering $\Lambda_U(\omega, T)$, and grain boundary scattering $\Lambda_B(\omega)$ as

$$\Lambda_{\text{eff}}^{-1}(\omega, T) = \Lambda_I^{-1}(\omega) + \Lambda_U^{-1}(\omega, T) + \Lambda_B^{-1}(\omega), \quad (10)$$

where $\Lambda_I^{-1}(\omega) = A_1 \omega^4/v_s$, and $\Lambda_U^{-1}(\omega, T) = B_1 \omega^2 T e^{-B_2/T}/v_s$ ²⁷; A_1 , B_1 , and B_2 are fitting parameters. We use $A_1 = 1.69 \times 10^{-45} \text{ s}^3$, $B_1 = 1.53 \times 10^{-19} \text{ sK}^{-1}$, and $B_2 = 140 \text{ K}$, the same as those used by Wang et al. for bulk *nc*-Si with $D = 76$ –550 nm (ref. 27) and subsequently by us for our HWCVD *nc*-Si with $D = 9.7 \text{ nm}$ (ref. 29).

Data availability

The data that support the findings of this study are available from the authors on reasonable request, see author contributions for specific data sets.

Received: 7 December 2020; Accepted: 2 June 2021;

Published online: 23 July 2021

References

- Haras, M. et al. Thermoelectric energy conversion: how good can silicon be? *Mater. Lett.* **157**, 193–196 (2015).
- Bennett, N. S. Thermoelectric performance in n-type bulk silicon: the influence of dopant concentration and dopant species. *Phys. Status Solidi A* **214**, 1700307 (2017).
- Dehkordi, A. M., Zebarjadi, M., He, J. & Tritt, T. M. Thermoelectric power factor: enhancement mechanisms and strategies for higher performance thermoelectric materials. *Mate. Sci. Eng. R Rep.* **97**, 1–22 (2015).
- Bux, S. K. et al. Nanostructured bulk silicon as an effective thermoelectric material. *Adv. Func. Mater.* **19**, 2445–2452 (2009).
- Kessler, V. et al. Thermoelectric properties of nanocrystalline silicon from a scaled-up synthesis plant. *Adv. Eng. Mater.* **15**, 379–385 (2013).
- Claudio, T. et al. Nanocrystalline silicon: lattice dynamics and enhanced thermoelectric properties. *Phys. Chem. Chem. Phys.* **16**, 25701–25709 (2014).
- Schierning, G. et al. Concepts for medium-high to high temperature thermoelectric heat-to-electricity conversion: a review of selected materials and basic considerations of module design. *Transl. Mater. Res.* **2**, 025001 (2015).
- Fitriani et al. A review on nanostructures of high-temperature thermoelectric materials for waste heat recovery. *Renew. Sustain. Energy Rev.* **64**, 635–659 (2016).
- Dames, C. & Chen, G. Theoretical phonon thermal conductivity of si/ge superlattice nanowires. *J. Appl. Phys.* **95**, 682–693 (2004).
- Chen, G. Thermal conductivity and ballistic-phonon transport in the cross-plane direction of superlattices. *Phys. Rev. B* **57**, 14958–14973 (1998).
- Yang, F. & Dames, C. Mean free path spectra as a tool to understand thermal conductivity in bulk and nanostructures. *Phys. Rev. B* **87**, 035437 (2013).
- Liu, W. & Asheghi, M. Thermal conductivity measurements of ultra-thin single crystal silicon layers. *J. Heat. Trans.* **128**, 75–83 (2006).
- Chavez-Angel, E. et al. Reduction of the thermal conductivity in free-standing silicon nano-membranes investigated by non-invasive raman thermometry. *APL Mater.* **2**, 012113 (2014).
- Neogi, S. et al. Tuning thermal transport in ultrathin silicon membranes by surface nanoscale engineering. *ACS Nano* **9**, 3820–3828 (2015).
- Li, D. et al. Thermal conductivity of individual silicon nanowires. *Appl. Phys. Lett.* **83**, 2934–2936 (2003).
- Hochbaum, A. I. et al. Enhanced thermoelectric performance of rough silicon nanowires. *Nature* **451**, 163 (2008).
- Wingert, M. C. et al. Thermal conductivity of ge and ge-si core-shell nanowires in the phonon confinement regime. *Nano Lett.* **11**, 5507–5513 (2011).
- Lim, J., Hippalgaonkar, K., Andrews, S. C., Majumdar, A. & Yang, P. Quantifying surface roughness effects on phonon transport in silicon nanowires. *Nano Lett.* **12**, 2475–2482 (2012).
- Murphy, K. F., Piccione, B., Zanjani, M. B., Lukes, J. R. & Gianola, D. S. Strain- and defect-mediated thermal conductivity in silicon nanowires. *Nano Lett.* **14**, 3785–3792 (2014).
- Wingert, M. C. et al. Sub-amorphous thermal conductivity in ultrathin crystalline silicon nanotubes. *Nano Lett.* **15**, 2605–2611 (2015).
- Zhao, Y. et al. Engineering the thermal conductivity along an individual silicon nanowire by selective helium ion irradiation. *Nat. Commun.* **8**, 15919 (2017).
- Yu, J.-K., Mitrovic, S., Tham, D., Varghese, J. & Heath, J. R. Reduction of thermal conductivity in phononic nanomesh structures. *Nat. Nanotechnol.* **5**, 718–721 (2010).
- Tang, J. et al. Holey silicon as an efficient thermoelectric material. *Nano Lett.* **10**, 4279–4283 (2010).
- Perez-Taborda, J. A., Muñoz Rojo, M., Maiz, J., Neophytou, N. & Martin-Gonzalez, M. Ultra-low thermal conductivities in large-area si-ge nanomeshes for thermoelectric applications. *Sci. Rep.* **6**, 32778 (2016).
- Zhao, Y. et al. Ultralow thermal conductivity of single crystalline porous silicon nanowires. *Adv. Funct. Mater.* **27**, 1702824 (2017).
- Ferrando-Villalba, P. et al. Impact of pore anisotropy on the thermal conductivity of porous si nanowires. *Sci. Rep.* **8**, 12796 (2018).
- Wang, Z., Alaniz, J. E., Jang, W., Garay, J. E. & Dames, C. Thermal conductivity of nanocrystalline silicon: importance of grain size and frequency-dependent mean free paths. *Nano Lett.* **11**, 2206–2213 (2011).
- Uma, S., McConnell, A. D., Asheghi, M., Kurabayashi, K. & Goodson, K. E. Temperature-dependent thermal conductivity of undoped polycrystalline silicon layers. *Int. J. Thermophys.* **22**, 605–616 (2001).
- Jugdersuren, B. et al. Thermal conductivity of amorphous and nanocrystalline silicon films prepared by hot-wire chemical-vapor deposition. *Phys. Rev. B* **96**, 014206 (2017).
- de Boor, J. et al. Temperature and structure size dependence of the thermal conductivity of porous silicon. *Europhys. Lett.* **96**, 16001 (2011).
- Cahill, D. G., Fisher, H. E., Klitsner, T. & Swartz, E. T. *J. Vac. Sci. Technol. A* **7**, 1259 (1989).
- Basu, R. et al. Improved thermoelectric performance of hot pressed nanostructured n-type si-ge bulk alloys. *J. Mater. Chem. A* **2**, 6922–6930 (2014).
- Pernot, G. et al. Precise control of thermal conductivity at the nanoscale through individual phonon-scattering barriers. *Nat. Mater.* **9**, 491–495 (2010).

34. Costescu, R. M., Cahill, D. G., Fabreguette, F. H., Sechrist, Z. A. & George, S. M. Ultra-low thermal conductivity in w/al2o3 nanolaminates. *Science* **303**, 989–990 (2004).
35. Chiritescu, C. et al. Ultralow thermal conductivity in disordered, layered wse2 crystals. *Science* **315**, 351–353 (2007).
36. Feser, J. P., Chan, E. M., Majumdar, A., Segalman, R. A. & Urban, J. J. Ultralow thermal conductivity in polycrystalline cds thin films with controlled grain size. *Nano Lett.* **13**, 2122–2127 (2013).
37. Agne, M. T., Hanus, R. & Snyder, G. J. Minimum thermal conductivity in the context of diffusion-mediated thermal transport. *Energy Environ. Sci.* **11**, 609–616 (2018).
38. Loureiro, J. et al. Improved thermoelectric properties of nanocrystalline hydrogenated silicon thin films by post-deposition thermal annealing. *Thin Solid Films* **642**, 276–280 (2017).
39. Miura, A., Zhou, S., Nozaki, T. & Shiomi, J. Crystalline-amorphous silicon nanocomposites with reduced thermal conductivity for bulk thermoelectrics. *ACS Appl. Mater. Interfaces* **7**, 13484–13489 (2015).
40. Oyake, T. et al. Ultimate confinement of phonon propagation in silicon nanocrystalline structure. *Phys. Rev. Lett.* **120**, 045901 (2018).
41. Kroll, U., Meier, J., Shah, A., Mikhailov, S. & Weber, J. Hydrogen in amorphous and microcrystalline silicon films prepared by hydrogen dilution. *J. Appl. Phys.* **80**, 4971–4975 (1996).
42. Fu, Y. Q., Luo, J. K., Milne, S. B., Flewitt, A. J. & Milne, W. I. Residual stress in amorphous and nanocrystalline si films prepared by pecvd with hydrogen dilution. *Mater. Sci. Eng. B* **124–125**, 132–137 (2005).
43. Matsuda, A. *Amorphous and Microcrystalline Silicon*, 573–587 (Springer International Publishing, 2017).
44. Kearney, B. T. et al. From amorphous to nanocrystalline: the effect of nanograins in an amorphous matrix on the thermal conductivity of hot-wire chemical-vapor deposited silicon films. *J. Condens. Matter Phys.* **30**, 085301 (2018).
45. Wei, W., Xu, G., Wang, J. & Wang, T. Raman spectra of intrinsic and doped hydrogenated nanocrystalline silicon films. *Vacuum* **81**, 656–662 (2007).
46. Koh, Y. K. & Cahill, D. G. Frequency dependence of the thermal conductivity of semiconductor alloys. *Phys. Rev. B* **76**, 075207 (2007).
47. Cahill, D. G., Katiyar, M. & Abelson, J. R. Thermal conductivity of a-si: H thin films. *Phys. Rev. B* **50**, 6077 (1994).
48. Zink, B. L., Pietri, R. & Hellman, F. Thermal conductivity and specific heat of thin-film amorphous silicon. *Phys. Rev. Lett.* **96**, 055902 (2006).
49. Liu, X. et al. High thermal conductivity of a hydrogenated amorphous silicon film. *Phys. Rev. Lett.* **102**, 035901 (2009).
50. Yang, H.-S. et al. Anomalously high thermal conductivity of amorphous si deposited by hot-wire chemical vapor deposition. *Phys. Rev. B* **81**, 104203 (2010).
51. Liu, X. et al. Internal friction of amorphous and nanocrystalline silicon at low temperatures. *Mater. Sci. Eng. A* **442**, 307–313 (2006).
52. Hori, T., Shiomi, J. & Dames, C. Effective phonon mean free path in polycrystalline nanostructures. *Appl. Phys. Lett.* **106**, 171901 (2015).
53. Maldovan, M. Thermal energy transport model for macro-to-nanograin polycrystalline semiconductors. *J. Appl. Phys.* **110**, 114310 (2011).
54. Dong, H., Wen, B. & Melnik, R. Relative importance of grain boundaries and size effects in thermal conductivity of nanocrystalline materials. *Sci. Rep.* **4**, 7037 (2014).
55. Bodapati, A., Schelling, P. K., Phillpot, S. R. & Keblinski, P. Vibrations and thermal transport in nanocrystalline silicon. *Phys. Rev. B* **74**, 245207 (2006).
56. Ju, S. & Liang, X. Thermal conductivity of nanocrystalline silicon by direct molecular dynamics simulation. *J. Appl. Phys.* **112**, 064305 (2012).
57. Braun, J. L. et al. Size effects on the thermal conductivity of amorphous silicon thin films. *Phys. Rev. B* **93**, 140201 (2016).
58. Kwon, S., Zheng, J., Wingert, M. C., Cui, S. & Chen, R. Unusually high and anisotropic thermal conductivity in amorphous silicon nanostructures. *ACS Nano* **11**, 2470–2476 (2017).
59. Allen, P. B., Feldman, J. L., Fabian, J. & Wooten, F. Diffusions, locons and propagons: character of atomic vibrations in amorphous si. *Philos. Mag.* **B 79**, 1715–1731 (1999).
60. Zhou, Y. & Hu, M. Record low thermal conductivity of polycrystalline si nanowire: breaking the casimir limit by severe suppression of propagons. *Nano Lett.* **16**, 6178–6187 (2016).
61. Lee, J.-H., Galli, G. A. & Grossman, J. C. Nanoporous si as an efficient thermoelectric material. *Nano Lett.* **8**, 3750–3754 (2008).
62. He, Y., Donadio, D., Lee, J.-H., Grossman, J. C. & Galli, G. Thermal transport in nanoporous silicon: Interplay between disorder at mesoscopic and atomic scales. *ACS Nano* **5**, 1839–1844 (2011).
63. Gesele, G., Linsmeier, J., Drach, V., Fricke, J. & Arens-Fischer, R. Temperature-dependent thermal conductivity of porous silicon. *J. Phys. D: Appl. Phys.* **30**, 2911 (1997).
64. Song, D. & Chen, G. Thermal conductivity of periodic microporous silicon films. *Appl. Phys. Lett.* **84**, 687–689 (2004).
65. Alvarez, F. X., Jou, D. & Sellitto, A. Pore-size dependence of the thermal conductivity of porous silicon: a phonon hydrodynamic approach. *Appl. Phys. Lett.* **97**, 033103 (2010).
66. Bera, C., Mingo, N. & Volz, S. Marked effects of alloying on the thermal conductivity of nanoporous materials. *Phys. Rev. Lett.* **104**, 115502 (2010).
67. Sellitto, A., Jou, D. & Cimmelli, V. A. A phenomenological study of pore-size dependent thermal conductivity of porous silicon. *Acta Appl. Math.* **122**, 435–445 (2012).
68. Vargiamidis, V. & Neophytou, N. Hierarchical nanostructuring approaches for thermoelectric materials with high power factors. *Phys. Rev. B* **99**, 045405 (2019).
69. Chakraborty, D., de Sousa Oliveira, L. & Neophytou, N. Enhanced phonon boundary scattering at high temperatures in hierarchically disordered nanostructures. *J. Electron. Mater.* **48**, 1909–1916 (2019).
70. Thanh Tung, B. & Mau Chien, D. Control of crystalline volume and nano crystal grain size in nanocrystalline silicon thin film deposited by pecvd. *Eur. Phys. J. Appl. Phys.* **68**, 20303 (2014).

Acknowledgements

We thank Zhe Cheng, Xiaoyang Ji, and D.G. Cahill for sound velocity measurements. This work is supported by the Office of Naval Research.

Author contributions

B.J. conceived the thermal conductivity experiments, and together with B.T.K. carried it out. Raman data were taken by J.C.C. X-ray diffraction data were taken by C.N.C. High-angle annular dark-field images of cross-sectional scanning transmission electron microscope were taken by M.B.K. and R.M.S. Data analysis of thermal conductivity was performed by B.J. and X.L. The paper was written by X.L. with input from all authors.

Competing interests

The authors declare no competing interests.

Additional information

Supplementary information The online version contains supplementary material available at <https://doi.org/10.1038/s42005-021-00662-9>.

Correspondence and requests for materials should be addressed to B.J. or X.L.

Peer review information *Communications Physics* thanks the anonymous reviewers for their contribution to the peer review of this work. Peer reviewer reports are available.

Reprints and permission information is available at <http://www.nature.com/reprints>

Publisher's note Springer Nature remains neutral with regard to jurisdictional claims in published maps and institutional affiliations.



Open Access This article is licensed under a Creative Commons Attribution 4.0 International License, which permits use, sharing, adaptation, distribution and reproduction in any medium or format, as long as you give appropriate credit to the original author(s) and the source, provide a link to the Creative Commons license, and indicate if changes were made. The images or other third party material in this article are included in the article's Creative Commons license, unless indicated otherwise in a credit line to the material. If material is not included in the article's Creative Commons license and your intended use is not permitted by statutory regulation or exceeds the permitted use, you will need to obtain permission directly from the copyright holder. To view a copy of this license, visit <http://creativecommons.org/licenses/by/4.0/>.

This is a U.S. Government work and not under copyright protection in the US; foreign copyright protection may apply 2021